A Technique to Infer Magnetic Topology at Mars and Its Application to the Terminator Region

Shaosui Xu, Tristan Weber, David L. Mitchell, David A. Brain, Christian Mazelle, Gina A. Dibraccio, Jared Espley

JGR Space Physics

RESEARCH ARTICLE

Key Points:
- A technique combining e- pitch angle and energy distribution is developed to most accurately infer up to seven magnetic topologies at Mars
- Closed magnetic loops with trapped electrons occur frequently over stronger crustal field regions at higher altitudes
- Cross-terminator closed loops are more spatially confined over strong crustal regions and distantly separated over weak crustal regions

Supporting Information:
- Supporting Information S1

Correspondence to:
S. Xu,
shaosui.xu@ssl.berkeley.edu

Citation:

A Technique to Infer Magnetic Topology at Mars and Its Application to the Terminator Region

Shaosui Xu[1] ID, **Tristan Weber**[2] ID, **David L. Mitchell**[1] ID, **David A. Brain**[2] ID, **Christian Mazelle**[3] ID, **Gina A. DiBraccio**[4] ID, and **Jared Espley**[4] ID

[1]Space Sciences Laboratory, University of California, Berkeley, CA, USA, [2]Laboratory for Atmospheric and Space Physics, University of Colorado Boulder, Boulder, CO, USA, [3]IRAP, CNRS-University of Toulouse-UPS-CNES, Toulouse, France, [4]Goddard Space Flight Center, Greenbelt, MD, USA

Abstract Magnetic topology is important for understanding the Martian plasma environment, including particle precipitation, energy transport, cold ion escape, and wave-particle interaction. In this study, we combine two independent but complementary methods in order to determine magnetic topology based on superthermal electron energy and pitch angle distributions. This approach removes ambiguities that result from using either energy or pitch angle alone, providing a more accurate and comprehensive determination of magnetic topology than previous studies. By applying this combined technique, we are able to identify seven magnetic topologies, including four types of closed field lines, two types of open field lines, and draped. All seven topologies are present in the Mars environment and are mapped in longitude, latitude, solar zenith angle, and altitude with the combined technique near the terminator. We find that closed field lines with double-sided loss cones are frequently present over stronger crustal field regions at higher altitudes. We also show that the cross-terminator closed field lines are more spatially confined over strong crustal regions, likely connecting nearby magnetic crustal patches. In contrast, cross-terminator closed loops over weak crustal regions have more distantly separated foot points, most likely connecting distant crustal patches.

1. Introduction

The interaction of solar wind and the Mars′ ionosphere, along with strong localized crustal magnetic fields (e.g., Acuña et al., 1998; Acuna et al., 1999; Brain et al., 2003; Connerney et al., 2005; Connerney, Espley, DiBraccio, et al., 2015), gives rise to a complex and dynamic magnetic topology (e.g., Brain et al., 2005, 2007; Lillis & Brain, 2013; Weber et al., 2017; Xu, Mitchell, Liemohn, et al., 2017) through plasma processes such as magnetic reconnection (e.g., Eastwood et al., 2008; Halekas et al., 2009; Harada et al., 2017, 2018). Magnetic topology is generally categorized into three types: (1) closed with both ends embedded in the collisional atmosphere, (2) open with one end connecting to the solar wind and the other intersecting the collisional atmosphere, and (3) draped that connects to the solar wind on both ends.

Magnetic topology is important for understanding the Martian plasma environment. First, as electrons and low-energy ions are magnetized above the collisional atmosphere, magnetic topology is important for characterizing energetic electron precipitation and low-energy ion escape. More specifically, solar wind electrons and solar energetic particle electrons can precipitate along open field lines (e.g., Dubinin, Fraenz, Woch, Winningham, et al., 2008; Dubinin, Fraenz, Woch, Roussos, et al., 2008; Lillis & Brain, 2013; Lillis et al., 2009, 2011, 2018; Xu et al., 2014), and ionospheric photoelectrons can precipitate onto the nightside atmosphere along cross-terminator closed field lines (e.g., Liemohn et al., 2007; Ulusen et al., 2011; Xu, Mitchell, et al., 2016; Xu, Mitchell, Liemohn, et al., 2017), causing heating (e.g., Fox & Dalgarno, 1979; Sakai et al., 2016), ionization (e.g., Adams et al., 2018; Cui et al., 2018; Fillingim et al., 2007, 2010; Xu, Mitchell, et al., 2016), and auroral emission (e.g., Bertaux et al., 2005; Brain et al., 2006; Haider et al., 1992; Leblanc et al., 2006, 2008; Schneider et al., 2015, 2018; Seth et al., 2002; Shane et al., 2016). At the same time, low-energy ions can escape along open field lines (e.g., Ergun et al., 2015; Jakosky et al., 2018), accelerated partly by ambipolar electric fields (e.g., Collinson et al., 2015; Xu, Mitchell, et al., 2018), and on draped field lines through the $\mathbf{J} \times \mathbf{B}$ force and/or the convection electric field (e.g., Cravens et al., 2017; Fang et al., 2008; Halekas, Brain, et al., 2017). In addition, the magnetotail and tail current sheet configuration is likely impacted by magnetic topology (e.g., DiBraccio et al., 2018; Frahm et al., 2010; Luhmann et al., 2015; Liemohn & Xu,
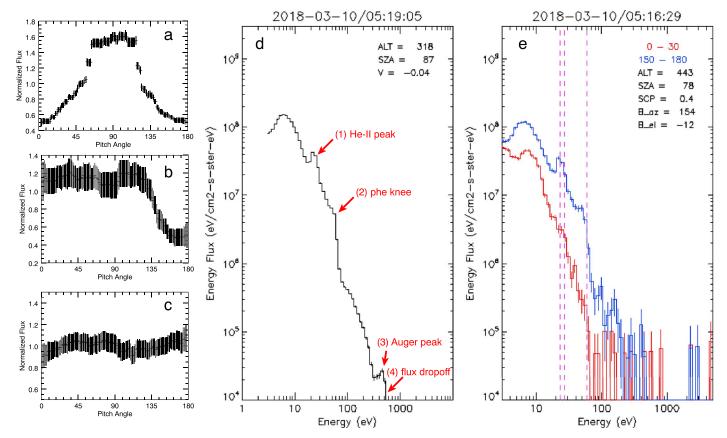
Figure 1. (a–c) Pitch angle distributions, reproduced from Figure 2 of Weber et al. (2017), for double-sided loss cone (a), one-sided loss cone (b), and isotropic (c). (d) An omnidirectional energy spectrum for photoelectrons from SWEA; (f) SWEA energy spectra separated for pitch angles 0–30° and 150–180°. SZA = solar zenith angle; SWEA = Solar Wind Electron Analyzer.

2018; Liemohn et al., 2017; Xu, Mitchell, Luhmann, et al., 2017). Finally, anisotropic electron distributions on open or closed field lines can generate narrowband whistler mode waves, which can cause electron scattering and precipitation (Harada et al., 2016).

Superthermal electrons (>~1 eV) are good magnetic tracers, as they are typically magnetized (with guiding center motions following the magnetic field lines) above altitudes where collisions with neutral particles are negligible. Because of their fast speeds (1 eV ~ 600 km/s), traveling thousands of kilometers within seconds, superthermal electrons can be used to infer the properties of the plasma source regions sampled by the magnetic field line at large distances from the spacecraft. At Mars, superthermal electrons mainly consist of ionospheric primary photoelectrons and solar wind origin electrons. The altitude above which electron transport dominates is defined as the superthermal electron exobase, located at ~160 km (e.g., Xu, Liemohn, Bougher, et al., 2015; Xu, Liemohn, et al., 2016). Below the exobase, the superthermal electron population is controlled by local productions and/or collisions with neutral particles and thermal plasma (<~1 eV). Therefore, magnetic topology inferred from superthermal electrons is valid only above the electron exobase, rather than down to the planet surface. However, magnetic topology defined this way can determine whether a field line has access to the collisional ionosphere, which suffices for many plasma physics topics.

The mapping of magnetic topology at Mars has mainly been conducted with two methods. One method is to examine electron pitch angle distributions (PADs; e.g., Brain et al., 2007; Weber et al., 2017). The presence of loss cones, or low electron fluxes near pitch angles of 0° and/or 180° (traveling parallel and/or antiparallel to the magnetic field), indicates atmospheric absorption and therefore that the field line intersects the collisional atmosphere on one or both ends. A double-sided loss cone (Figure 1a) indicates a closed field line; a one-sided loss cone (Figure 1b) indicates an open field line. With such a technique, Brain et al. (2007) and Weber et al. (2017) mapped out magnetic topology at Mars with measurements from the Magnetometer (MAG)/Electron Reflectometer instrument(Acuña et al., 1992; Mitchell et al., 2001) onboard

the Mars Global Surveyor (MGS) spacecraft and from the Solar Wind Electron Analyzer (SWEA; Mitchell et al., 2016), and MAG (Connerney, Espley, Lawton, et al., 2015) onboard the Mars Atmosphere and Volatile EvolutioN (MAVEN) spacecraft (Jakosky et al., 2015), respectively.

The other method of inferring magnetic topology is to identify the source region(s) of superthermal electrons traveling parallel or antiparallel to the field line by examining their energy distributions. Ionospheric photoelectrons can be distinguished from solar wind origin electrons through several energy spectral features (Figure 1d), corresponding to features in the solar spectrum (e.g., Peterson et al., 2016; Sakai et al., 2015; Xu, Liemohn, Peterson, et al., 2015): (1) a cluster of sharp peaks from 22 to 27 eV caused by the intense He-II 30.4 nm (~40 eV) ionizing CO_2 and O (e.g., Coates et al., 2011; Frahm, Sharber, et al., 2006; Frahm, Winningham, et al., 2006); (2) a large flux decrease from 60 to 70 eV ("the photoelectron knee") produced by a corresponding dropoff of solar irradiance at wavelengths < 17 nm (e.g., Shane et al., 2016; Xu et al., 2014); (3) Auger peaks near 250 eV and 500 eV produced by ionization of K-shell electrons in atomic carbon and oxygen, respectively, by soft X-rays (e.g., Mitchell et al., 2000; Xu, Thiemann, et al., 2018); (4) another sharp decrease in electron flux near 500 eV due to another drop in solar irradiance $<\sim 1 - 2$ nm(e.g., Liemohn et al., 2003; Xu & Liemohn, 2015). The presence of ionospheric photoelectrons traveling parallel and/or antiparallel to the magnetic field indicates that the field line has one or two foot points embedded in the dayside ionosphere. This technique has been used to map open and closed field lines connected to the dayside ionosphere in the Martian magnetotail (e.g., Coates et al., 2011; Frahm et al., 2010; Liemohn et al., 2006, 2006; Xu, Mitchell, Luhmann, et al., 2017), strong crustal magnetic field regions (e.g., Dubinin, Fraenz, Woch, Winningham, et al., 2008, Dubinin, Fraenz, Woch, Roussos, et al., 2008; Shane et al., 2016; Xu et al., 2014), throughout the near-Mars environment below 1,000-km altitude (e.g., Xu, Mitchell, Liemohn, et al., 2017), as well as for investigating the magnetic topology response to an interplanetary coronal mass ejection (ICME) event (Xu, Fang, et al., 2018).

A closely related method for inferring one specific topology is based on superthermal electron voids, where the measured flux drops by orders of magnitude, nearly to instrument background. These have been observed by MGS (e.g., Brain et al., 2007; Mitchell et al., 2001, 2007), Mars Express (e.g., Duru et al., 2011; Hall et al., 2016), and MAVEN (e.g., Steckiewicz et al., 2015, 2017; Weber et al., 2017; Xu, Mitchell, Liemohn, et al., 2017). This observation is interpreted as a closed field line with both foot points connected to the nightside atmosphere. Since there is no photoelectron production at the foot points because they are in darkness, and no path for the entry of solar wind electrons because the field line is closed, any superthermal electrons are continuously lost to the atmosphere, mainly due to collisions with neutral particles and thermal electrons. The locations of these electron voids are highly correlated with crustal magnetic field patterns (e.g., Brain et al., 2007; Hall et al., 2016; Mitchell et al., 2007; Steckiewicz et al., 2015, 2017; Weber et al., 2017; Xu, Mitchell, Liemohn, et al., 2017). Superthermal electron voids have already been incorporated into each of the two aforementioned methods by several studies (e.g., Brain et al., 2007; Weber et al., 2017; Xu, Mitchell, Liemohn, et al., 2017). Thus, the usage of electron voids is not labeled here as an independent method for convenience.

Studies based on each method have provided valuable insights into Martian magnetic topology and related topics. However, there exist ambiguities in each method alone. The pitch angle method relies on the presence of loss cones, which would be problematic for dayside observations for two reasons. First, if no loss cone is present, it could indicate either a draped field line populated with solar wind electrons or a closed field line populated with isotropic photoelectrons. Although, the maps of isotropic electron distributions on the dayside from MGS observations correspond to crustal magnetic field patterns, which indicates the latter scenario at 400 km (Brain et al., 2007). Second, for an open field line connected to the dayside, solar wind electrons precipitate onto the foot point and are absorbed while photoelectrons are produced at the foot point and flow upward. There are cases from MAVEN data where the downward and upward fluxes can be similar at 100–500 eV, so that a loss cone might be undetectable within this energy range. The energy method relies on the presence of photoelectrons so that it cannot distinguish a draped field line from an open field line connected to the nightside atmosphere, as photoelectrons are absent in both parallel and antiparallel directions in both cases. As one method has ambiguities on the dayside and the other on the nightside, combining them can provide the most accurate and comprehensive topology determination, which is the topic of this study. This combined technique is especially powerful for determining magnetic topology in complicated regions, such as near the terminator. Our particular application of this technique is optimized for electron measurements from SWEA, in combination with magnetic field data from MAG onboard MAVEN,
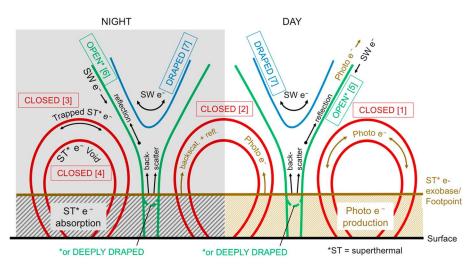
Figure 2. A schematic displaying the relationship of superthermal electrons and each magnetic topology. Red for closed, green for open or deeply draped (field line dips below the electron exobase but does not continue to the surface), and blue for draped. Up to seven topologies can be identified: (1) closed-to-day [C-D], (2) cross-terminator-closed [C-X], (3) closed-trapped [C-T], (4) voids [C-V], (5) open-to-day [O-D], (6) open-to-night [O-N], and (7) draped [DP]. The left half, shaded in gray, is for the nightside and the right half for the dayside. Below the superthermal electron exobase, there is photoelectron production on the dayside, while the nightside atmosphere is an absorber for superthermal electrons. Photo e- is short for photoelectrons, and SW e- for solar wind electrons.

although it is generally applicable whenever energy-angle electron distributions and magnetic field data are available. This paper is organized as follows: we describe the methodology in section 2, then map the terminator magnetic topology in section 3, and analyze the dominant topologies for strong and weak crustal field regions in section 4, followed by discussion and conclusions in section 5.

2. Methodology

2.1. Instruments

In this study, we use electron measurements from SWEA and magnetic field measurements from MAG onboard MAVEN, which has an elliptical orbit with a periapsis of ~150 km, an apoapsis of 2.8 Mars radii (R_M) and an orbit period of ~4.5 hr. The periapsis is occasionally lowered to ~120 km during week-long deep dip campaigns. The orbit inclination is 74° .

SWEA is a symmetric hemispheric electrostatic analyzer with deflectors and measures the energy-angular distribution of electrons from 3 to 2,000 eV for >80% of the sky and 2- to 4.6-keV electrons with a field of view that decreases with energy. SWEA has an energy resolution of $\Delta E/E = 16.7\%$ (full width at half maximum). The PAD data used in this study are 2-D cuts through the 3-D distributions that dynamically maximize the pitch angle coverage using real-time MAG data processed onboard the spacecraft and provided with a 2- to 4-s cadence. See more details about SWEA in Mitchell et al. (2016).

The MAG instrument is comprised of two independent triaxial fluxgate sensors located at the ends of the solar panels. Each magnetometer provides vector field measurements with an accuracy of 0.1 nT at a cadence of 1/32 s. See more details of MAG in Connerney, Espley, Lawton, et al. (2015).

2.2. Superthermal Electrons and Magnetic Topology

As described in the introduction, superthermal electrons are excellent magnetic tracers, although the inferred magnetic topology is only valid above the superthermal electron exobase, where we define the foot point(s) of a field line. Figure 2 depicts how we infer magnetic topology. In this study, we subdivide closed field lines into four types, open field lines into two types, and also identify draped field lines, making seven magnetic topologies in all. The direction of superthermal electron motion with respect to the planet is important for deducing magnetic topology. Therefore, we define the "away" direction to be electrons with a velocity directed away from Mars and "toward" to be electrons with a velocity directed toward Mars. This can be achieved by examining the elevation of the magnetic field, relative to the local horizontal plane,

and electron pitch angles (PAs). Pitch angle ranges of 0–30° and 150°–180° are chosen to determine away or toward in this study. In other words, for a positive magnetic elevation angle (the magnetic field points away from Mars), PA 0–30° is the away direction and PA 150–180° is the toward direction for electrons; for a negative magnetic elevation angle, PA 150–180° is the away direction and PA 0–30° is the toward direction for electrons. For measurements without pitch angle coverage in 0–30° and/or 150–180°, the topology is left to be "unknown." Note that the away and toward directions can be ambiguous when the magnetic field is nearly horizontal. In this study, we mainly conduct statistical analyses of magnetic topology so that occasional misidentifications should not significantly impact our results.

Closed field lines are red in Figure 2 and divided into four types. Topology 1 is a closed field line with both foot points embedded in the dayside ionosphere, the source region of photoelectrons. The signature of this topology is photoelectrons traveling in both the away and toward directions, as there is no solar wind plasma entry for such a topology and the field line is only populated by photoelectrons from the local ionosphere at each foot point. We label Topology 1 as "closed-to-day" or "C-D" in this study. For such a topology, there are photoelectrons in both field-aligned directions and no loss cone is formed in either direction. Topology 2 is a cross-terminator closed field line with one foot point on the dayside and the other on the nightside. Photoelectrons from the dayside ionosphere, in which the dayside foot point is embedded, precipitate onto the nightside atmosphere and are mostly absorbed by collisions with the neutral atmosphere and thermal electrons with a ∼30% backscatter rate (e.g., Collinson et al., 2016). The signature of this topology is different for dayside and nightside foot points: (1) away photoelectrons with a higher flux than toward backscattered electrons if observed near the dayside foot point; (2) toward photoelectrons with a higher flux than away backscattered electrons if observed near the nightside foot point. Thus, a loss cone is formed in the direction opposite to the source photoelectrons, that is, in the toward direction for the dayside foot point and in the away direction for the nightside foot point. We label Topology 2 as "cross-terminator-closed" or "C-X." On the nightside, there is no photoelectron production, so the atmosphere is mainly an absorber of superthermal electrons. Topology 3 is a closed field line with both foot points embedded in the nightside atmosphere, with superthermal electrons magnetically reflecting ("bouncing") above the exobase. The signature of this type is a double-sided loss cone, as field-aligned electrons are absorbed and electrons with pitch angles closer to 90° are trapped at high altitudes. We label Topology 3 as "closed-trapped" or "C-T." When the trapped electrons are scattered into the loss cone by processes such as electron-neutral collisions, they are lost to the atmosphere, and the result is a superthermal electron void, defined as Topology 4, or labeled as "voids"/"C-V" here. This process takes about 20 min on a closed loop once the source of superthermal electrons is turned off (Adams et al., 2018; Steckiewicz, 2017). As mentioned in section 1, the signature of this type is an electron flux close to the instrument background.

Open field lines are green in Figure 2 and divided into two types. The first category, or Topology 5, is an open field line intersecting the dayside ionosphere, labeled as "open-to-day"/"O-D." The signature of this topology is solar wind electrons precipitating onto the atmosphere in the toward direction and photoelectrons outflowing away from the planet. The backscattered solar wind electron flux is assumed to be lower than outflowing photoelectron flux, which is mostly the case under nominal solar wind conditions by inspection, especially for energies below the photoelectron knee. Topology 6 is an open field line intersecting the nightside atmosphere, with precipitating solar wind electrons in the toward direction and only backscattered electrons in the away direction (i.e., no photoelectrons in either direction), labeled as "open-to-night"/"O-N." This topology can be identified by a one-sided loss cone PAD. The inferred topology is only valid above the electron exobase, so that these "open" field lines can be deeply draped field lines that dip below the exobase but do not continue to the surface.

Draped field lines are blue in Figure 2, labeled as "draped"/"DP." This last topology (7) is identified by solar wind electrons in both field-aligned directions, as well as by the absence of loss cones in the away directions.

2.3. Technique

Now that we have described how to use superthermal electron information to infer magnetic topology, we introduce how to identify photoelectrons and loss cones with SWEA measurements, followed by how to combine this information to determine magnetic topology in practice.

2.3.1. Shape Parameter

Xu, Mitchell, Liemohn, et al. (2017) designed a shape parameter to identify photoelectrons with MAVEN data. We first obtain the derivative of the electron fluxes (F) with respect to energy (E) in log space
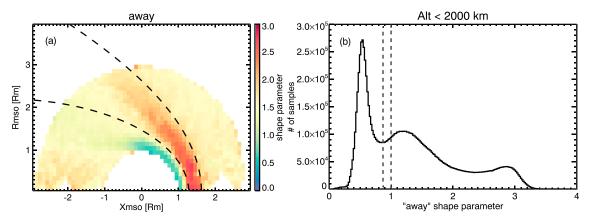
Figure 3. (a) The mapping of shape parameters for the "away" direction in the Mars-centered Solar Orbital (MSO) cylindrical coordinates. The dashed lines are conic section fits to the average bow shock and magnetic pileup boundary from Vignes et al. (2000). (b) The distribution of away-shape parameters below 2,000-km altitude. The two dashed lines mark the local minimum of shape parameters and the chosen threshold of 1.

$(d(\log F)/d(\log E))$ for an electron spectrum. The derivative is used to pick out sharp features in a photoelectron energy-flux spectrum, as described in section 1. The absolute difference of the derivatives from a measured electron spectrum and an ionospheric photoelectron spectrum template is calculated for each energy bin. We then sum the calculated absolute difference over 20 to 80 eV, so as to identify the He-II peak and photoelectron knee, which is defined as the shape parameter. Naturally, the smaller a shape parameter is, the more likely it is that it represents a photoelectron spectrum. More details of shape parameter can be found in Xu, Mitchell, Liemohn, et al. (2017).

The shape parameter is calculated separately for the away and toward directions. Figure 3a illustrates the away shape parameter mapped in the Mars-centered Solar Orbital (MSO) cylindrical coordinates (the distribution for the toward shape parameter is very similar, not shown here). In the MSO frame, X points from the center of Mars to the Sun, Y points opposite to the component of orbital motion perpendicular to the Mars-Sun line, and Z completes the right-handed system. Three distinct regions are revealed by the shape parameter: $<\sim$1 (photoelectrons) in the dayside ionosphere and extending into the tail along $R \sim$1, $>\sim$2 in the magnetosheath and roughly 1–2 in the magnetotail and upstream of the bow shock. Figure 3b shows the distribution of away-shape parameters below 2,000-km altitude. Three peaks can be identified, corresponding to different regions described above. The local minimum between photoelectrons and non-photoelectrons is located roughly at a shape parameter of $\sim$0.9, as indicated by the dashed line to the left in Figure 3b. In practice, we use a threshold of 1, the same as Xu, Mitchell, Liemohn, et al. (2017), to differentiate photoelectrons and nonphotoelectrons (backscattered electrons or solar wind origin electrons), as the electron spectrum might be a mixture of photoelectrons and solar wind origin electrons or a photoelectron spectrum degraded by collisions. The presence of photoelectrons defines the topology, regardless of whether they are mixed with backscattered solar wind electrons or degraded by collisions.

2.3.2. PAD Score

Following Weber et al. (2017), a PAD score is calculated as $(f_{FA} - f_{perp})/\sigma$, where f_{FA} and f_{perp} are the electron flux for field-aligned (the most field-aligned 10° available within PAs 0–30° or 150–180°) and perpendicular directions (PAs 85–95°) for 100- to 300-eV electrons (averaging electron fluxes for this energy range), and σ is a measurement of the propagated uncertainty in $(f_{FA} - f_{perp})$. Therefore, a loss cone corresponds to a negative PAD score, a beamed distribution corresponds to a positive PAD score, and an isotropic distribution corresponds to a score near zero (e.g., Figure 1c).

Similar to the shape parameter, the PAD score is calculated separately for away and toward directions. Figure 4 displays the away PAD score in the MSO cylindrical coordinates. Beamed distributions are seen mostly in the solar wind because of solar wind "strahl" electrons. Strong negative PAD scores in the magnetosheath region do not represent loss cones and are discussed in section 4.1. PAD scores are negative on average within the induced magnetosphere, corresponding to open field lines stretching out through the Martian tail. Here, we use a PAD score less than −3; that is, the field-aligned electron flux is 3σ smaller than the perpendicular electron flux, to detect a loss cone.
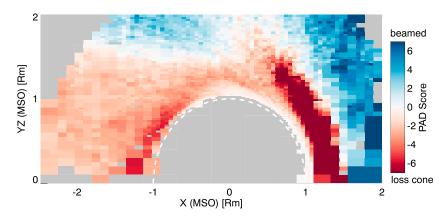
Figure 4. The mapping of pitch angle distribution (PAD) score for the "away" direction in the Mars-centered Solar Orbital (MSO) cylindrical coordinates. Negative values (< -3) correspond to loss cones and positive values to beamed distribution. Near zero represents isotropic distributions. The dashed half circle marks one Mars radius.

2.3.3. Combined Technique

Now that we have the shape parameter to separate photoelectrons and nonphotoelectrons (i.e., solar wind origin electrons or backscattered electrons) and the PAD score to identify loss cones, the relationship between these parameters and our seven magnetic topologies is detailed in Table 1.

Topologies 3 (C-T), 6 (O-N), and 7a (DP) are straightforward, just as illustrated in Figure 2. Following Xu, Mitchell, Liemohn, et al. (2017), a superthermal void (Topology 4, C-V) is defined as the energy flux of 40-eV electrons to be $< 10^5$ eV·cm^{-2}·s^{-1}·sr^{-1}·eV^{-1}, or roughly an order of magnitude above instrument background. This particular choice of a threshold results in some misidentifications of closed field lines near the terminator, where we identify a high concentration of draped topology below the electron exobase, because both shape parameter and PAD score fail due to a relative high noise-to-signal ratio. These closed loops have low 40-eV fluxes but still above our threshold, because there has been insufficient time in darkness for superthermal electrons to be absorbed by the atmosphere. They are in effect the precursors to voids. These regions are misidentified as draped by our technique because both the shape parameter and PAD score fail as a result of the low signal-to-noise ratio. Conversely, a higher threshold defeats the meaning of an electron void.

The differentiation of Topologies 1 (C-D), 2 (C-X), and 5 (O-D) is more complicated when we take into account the possible distortion of magnetic fields or locally horizontal magnetic fields, so that the away

Table 1
Illustration of How to Determine Seven Magnetic Topologies

Topo #	A-shape	T-shape	A-PAD score	T-PAD score	A/T ratio	Void (Y/N)	Region ID
1 C-D	Phe	Phe	—	—	$0.2 < r < 5$	N	—
2 C-X	[2a] Phe	Phe	—	—	$r > 5$ or r< 0.2	N	—
	[2b] Phe	SWe	No LC	LC	—	N	—
	[2c] SWe	Phe	LC	No LC	—	N	—
3 C-T	—	—	LC	LC	—	N	—
4 C-V	—	—	—	—	—	Y	—
5 O-D	[5a] Phe	SWe	—	No LC	—	N	—
	[5b] SWe	Phe	No LC	—	—	N	—
6 O-N	SWe	SWe	LC	No LC	—	N	—
7 DP	[7a] SWe	SWe	No LC	—	—	N	—
	[7b] —	—	—	—	—	—	1 or 2

Note. "A" and "T" stand for "away" and "toward," respectively, "LC" for "loss cone," "Phe" for photoelectrons, and "SWe" for solar wind/backscattered electrons. "Ratio" is calculated as the away electron flux divided by the toward flux for 35–60 eV.
[a,b,c] See text.

and toward directions are reversed. For a cross-terminator closed field line, backscattered photoelectrons can sometimes be identified as photoelectrons (shape parameter <1), sometimes not, depending on the flux level. As a result, cross-terminator-closed can be confused with closed-to-day or open-to-day if only shape parameters are used. Therefore, we supplement with other information to differentiate these three topologies. If the backscattered electron flux is high enough to be identified as photoelectrons by the shape parameter, it would be the same for closed-to-day from cross-terminator-closed in terms of shape parameters, as both field-aligned directions are identified as photoelectrons. To distinguish closed-to-day from "cross-terminator-closed," we examine the averaged electron flux ratio for 35–60 eV of these two field-aligned directions, as there should be a large flux ratio for "cross-terminator-closed" between the source and backscattered photoelectron fluxes but a ratio of ~1 for closed-to-day. As shown in Table 1, if the away electron flux divided by the toward flux is >5 or <0.2 (scenario 2a in Table 1), suggesting a source flux (in the away and toward direction, respectively) at least 5 times greater than the backscattered flux, we define it as cross-terminator-closed (C-X); otherwise, we define the measurement as closed-to-day (C-D). The backscattered flux is ~30% of a source flux from simulations (Collinson et al., 2016) but observationally the backscattering rate can be lower, for example, <~15% from Collinson et al. (2016). We adopt strict thresholds of 0.2 and 5 to suppress false positives.

If the backscattered electron flux is so low to not be identified as photoelectrons (shape parameter >1), the signature of away and toward shape parameters is the same for cross-terminator-closed (C-X) and open-to-day (O-D). We separate cross-terminator-closed (C-X) and open-to-day (O-D) by the presence/absence of loss cones. For a cross-terminator closed field line, while the source photoelectron is identified in one direction ("Phe" by shape parameter), the backscattered electrons will result in a loss cone distribution in the other direction (identified as "SWe" by shape parameter). This corresponds to scenarios 2b and 2c in Table 1. In contrast, for "open-to-day" (O-D), solar wind electrons precipitate as a source, and therefore, there should be no loss cones for the direction identified as SWe by shape parameter. For the direction of photoelectrons (Phe by shape parameter), it can be either identified as loss cones, if photoelectron fluxes are lower than solar wind electron fluxes, or no loss cones (photoelectron fluxes comparable or higher than solar wind electron fluxes). This corresponds to scenarios 5a and 5b in Table 1.

Finally, shape parameter and PAD score sometimes falsely identify photoelectrons and loss cone in the solar wind and magnetosheath regions. For this reason, we make no attempt to determine magnetic topology in these regions. To determine when the spacecraft is in the upstream solar wind or magnetosheath, we use magnetic field amplitude and fluctuations together with the ion density, temperature, and bulk flow (Halekas, Ruhunusiri, et al., 2017). All topologies in these two plasma regions are marked as draped. A region ID is used, which identifies regions like solar wind (1), magnetosheath (2), ionosphere (3), and magnetic lobes (4), based on typical magnetic field and ion density and velocity behaviors in each region by using MAG and Solar Wind Ion Analyzer ((Halekas et al., 2015)) data. All the magnetic topologies determined above are overwritten as draped if the region ID is 1 or 2 (scenario 7b in Table 1).

2.3.4. Orbit Example

To demonstrate our combined technique, we show an orbit on 10 March 2018 in Figure 5, of which the periapsis was located over the southern hemisphere and past the terminator. The ephemeris information is listed at the bottom of the figure. The inferred magnetic topologies are shown in panels (g) and (h) by numbering and colors, respectively. For when there is no sufficient pitch angle coverage, we define the topology as "0-unknown." We choose examples for each topology, marked by the seven vertical dotted lines labeled with corresponding topologies in Figure 5h. Closed-to-day (1 C-D, Figure 5h) is identified by shape parameters <1 for both the away and toward directions (Figure 5d) and an away-to-toward flux ratio near 1 (Figure 5e). The He-II peak can also been seen as a distinct horizontal red line at ~23 eV in Figure 5j. For cross-terminator-closed (2 C-X), the conditions include the following: shape parameters <1 (photoelectrons) for both away and toward directions (Figure 5d) and an away-to-toward flux ratio of ~10 (Figure 5e). This corresponds to scenario 2a in Table 1. The electron energy spectra for this time are also shown in Figure 1e, where the source electrons (the blue spectrum) have a much higher flux than the backscattered electrons (the red spectrum). Closed with trapped electrons (3 C-T) is identified by a PAD score <−3 for both away and toward directions (Figure 5c). This and other trapped populations are apparent in Figure 5i by low fluxes at pitch angles near 0° and 180°. Voids (4 C-V) are identified with very low electron fluxes (Figure 5j).

Open-to-day (5 O-D) can be identified between 05:14 and 05:16. In Figure 5d, the away shape parameter is <1, indicating outflowing photoelectrons, while the toward shape parameter is >1, indicating precipitating
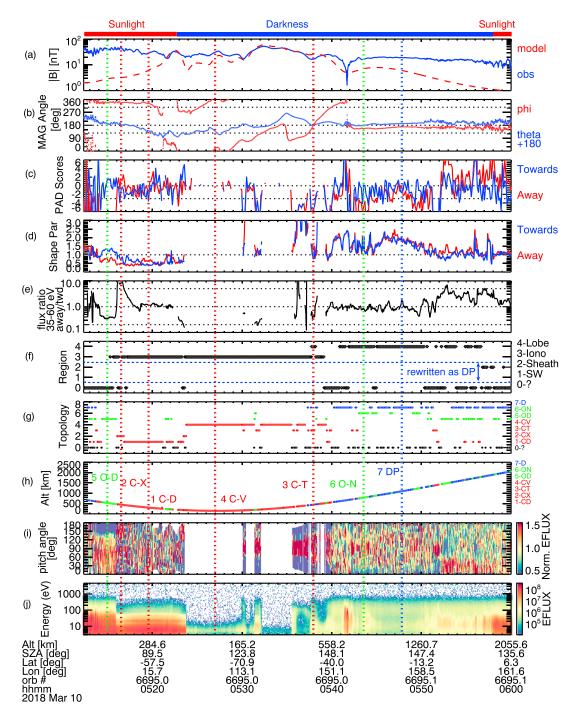
Figure 5. Time series of Mars Atmosphere and Volatile EvolutioN observations on 10 March 2018. From top to bottom: a color bar for spacecraft in darkness or sunlight, (a) magnetic field magnitude measured by Magnetometer (blue) and the modeled crustal magnetic field magnitude (Morschhauser et al., 2014; red), (b) magnetic angles in Mars-centered Solar Orbital (the phi angle is the azimuthal angle in Mars-centered Solar Orbital, pointing from *X* axis to *Y* axis, and the theta angle is the elevation angle relative to the *X*-*Y* plane but shifted by 180°), (c) pitch angle distribution (PAD) scores for "away" and "toward" directions, (d) shape parameters for away and toward directions, (e) the ratio of away and toward electron flux for 35–60 eV, (f) region ID (0: unknown, 1: solar wind, 2: magnetosheath, 3: ionosphere, and 4: magnetic lobes), (g) topology index (0: unknown and 1: closed-to-day [C-D], 2: cross-terminator-closed [C-X], 3: closed-trapped [C-T], 4: voids [C-V], 5: open-to-day [O-D], 6: open-to-night [O-N], 7: draped [DP]), (h) spacecraft altitude colored by magnetic topologies (red for all types of closed field lines, green for both types of open, blue for draped), (i) PAD of 111- to 140-eV electrons normalized by the median electron flux, and (j) electron energy spectra (in differential energy flux: eV·sr⁻¹·cm⁻²·s⁻¹·eV⁻¹) measured by Solar Wind Electron Analyzer.
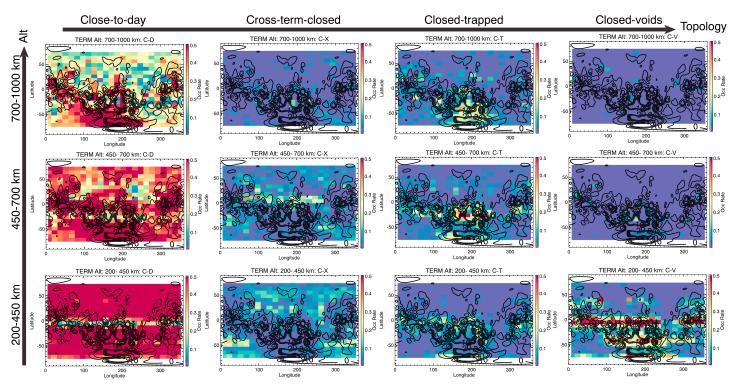
Figure 6. The occurrence rate of four types (four columns) of closed field lines in geographic maps for three altitude ranges, 200–450 km (bottom), 450–700 km (middle), 700–1,000 km (top), for 80 < SZA < 120. From left to right, four columns are closed-to-day (Topology 1, C-D), cross-terminator closed (Topology 2, C-X), closed-trapped (Topology 3, C-T), and voids (Topology 4, C-V). The line contours are the radial crustal magnetic fields at 400 km based on Morschhauser et al. (2014), from −30 to 30 nT, the same as in Figures 7 and 8.

solar wind electrons. In Figure 5c, the toward PAD score is ~1, representing no loss cone in toward direction, while the away PAD score is < −6, representing a loss cone in the away direction. The one-sided loss cones can also be seen in Figure 5i. Open-to-night (6 O-N) can be identified between 05:43 and 05:44. In Figure 5d, shape parameters are >1 for both away and toward directions. In Figure 5c, the away PAD score is < −3, representing a loss cone in the away direction, and the toward PAD score is > −3, representing no loss cone in toward direction. A to the very narrow one-sided loss cone (PA 0–10°) can be seen in Figure 5i at this time.

Finally, an example of the draped topology (7 DP) can be seen between 05:47 and 05:49. In both the away and toward directions, shape parameters are >1 (Figure 5d) and PAD scores are > −3 (Figure 5c), interpreted as solar wind electrons and no loss cone in both directions.

3. Magnetic Topology Near the Terminator (80° < SZA < 120°)

In this section, we apply our technique to magnetic topology near the terminator (80° < SZA [solar zenith angle] <120°), a complex region deliberately omitted in previous studies (e.g., Brain et al., 2007; Xu, Mitchell, Liemohn, et al., 2017), because of the different sources and sinks on the two ends of the field line so that how to infer each type with superthermal electrons is more complicated. SWEA and MAG data used in sections 3 and 4 are from 1 December 2014 to 28 February 2018. The total sample number for all topologies is shown in Figure S1 in the supporting information. All the SWEA data are corrected for spacecraft potentials, which is estimated based on a combination of the current-voltage characteristics from the Langmuir probe and waves instrument (Andersson et al., 2015), ion measurements from the suprathermal, and thermal ion composition instrument (McFadden et al., 2015), and electron measurements from SWEA.

3.1. Closed
Figure 6 shows the occurrence rates of four types of closed field lines (Topologies 1-4, C-D, C-X, C-T, and C-V) near the terminator as a function of geographic latitude and longitude from 200 to 1,000 km. Closed-to-day (Topology 1, C-D, the left column) has an occurrence rate of >50% below 700 km over most of the planet, except over areas with very weak crustal magnetic fields, and remains the dominant topology (>50%) over
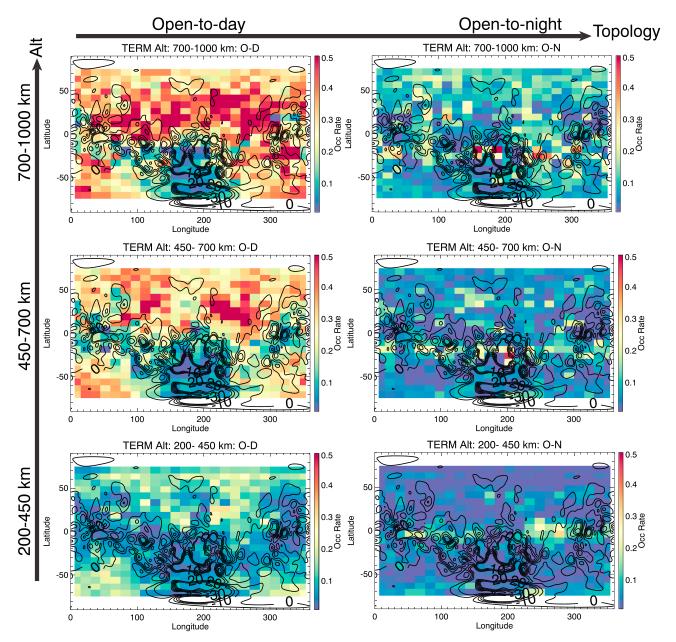
Figure 7. The occurrence rate of two types of open field lines in geographic maps for three altitude ranges, 200–450 km (bottom), 450–700 km (middle), and 700–1,000 km (top), for 80 < SZA < 120. The left column is for open-to-day (Topology 5, O-D) and right for open-to-night (Topology 6, O-N).

strong crustal magnetic fields at 1,000 km. The solar wind dynamic pressure, which varies with SZA as $\cos^2(SZA)$ (e.g., Crider et al., 2003) is small near the terminator so that crustal fields are less compressed, and the magnetic pileup boundary (e.g., Crider et al., 2002) and the photoelectron boundary (e.g., Garnier et al., 2017) is located at a higher altitude than in the subsolar region. Therefore, the occurrence rate for closed-to-day is slightly higher than that from Xu, Mitchell, Liemohn, et al. (2017). It is also worth mentioning that closed-to-day magnetic loops have been observed at large distances (up to MAVEN's apoapsis) down tail, as a result of either reconnection or distortion by the day-to-night plasma flow (Xu, Mitchell, Luhmann, et al., 2017).

Cross-terminator closed (Topology 2, C-X) has an occurrence rate <30%, which decreases with altitude (the second column of Figure 6). These closed loops are located over weak crustal fields at low altitudes and in the periphery of strong crustal fields at high altitudes, but not directly over strong crustal fields. This will be discussed in section 4.
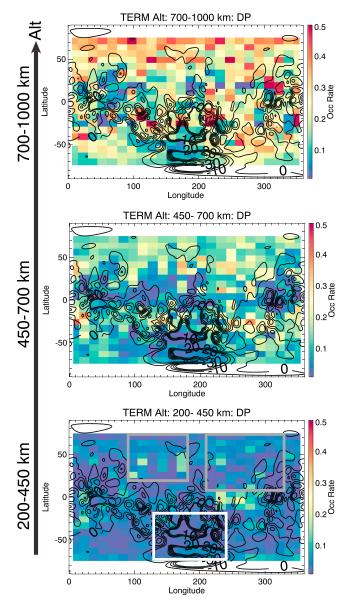
Figure 8. The occurrence rate of draped field lines (Topology 7, DP) for three altitude ranges, 200–450 km (bottom), 450–700 km (middle), and 700–1,000 km (top), for 80 < SZA < 120. The white box in the bottom left panel highlights a region of strong crustal fields and two gray boxes for weak crustal regions for section 4.

Closed-trapped (Topology 3, C-T) are associated with strong crustal fields, with a maximum occurrence rate of ~30% for each altitude range (the third column of Figure 6). The high occurrence rate pattern of this topology moves from weaker crustal regions to stronger crustal regions as altitude increases. This topology is more likely to be observed at high altitudes of closed loops, where electrons are trapped (magnetically reflecting above the exobase). Obviously, closed loops reach higher altitudes over strong crustal magnetic regions.

Superthermal electron voids (Topology 4, C-V) are mostly located below 450 km over strong crustal regions (the fourth column of Figure 6), which agrees with previous studies. The band-like high occurrence rate patterns (strips of high occurrence rates at latitudes near 0°, −40°, and −70°) are most likely caused by the sampling bias. MAVEN's sampling is more longitudinally uniform as Mars rotates underneath but the periapsis varies in latitude as time evolves. Our SZA range of 80–120° includes samples both before and past the terminator but voids should be only observed past the terminator. The three latitude bands with high

occurrence rates of voids are likely to be when MAVEN's periapsis is located behind the terminator and other latitude bands before the terminator within 80° < SZA < 120°.

3.2. Open

The occurrence rates of two types of open field lines are displayed in Figure 7. The occurrence rate of open-to-day (Topology 5, O-D) increases with altitude, up to ~50% in the 700- to 1,000-km altitude range, and is higher over weak crustal fields (the left column of Figure 7). Open-to-day becomes the dominant magnetic topology at some locations (compare Figures 6, 7, 8). This is because most of open field lines on the dayside extend past the terminator, bypassing strong crustal fields and clustering over weak crustal fields.

Naturally, open-to-night (Topology 6, O-N) accounts for <30% of topologies near the terminator (the right column of Figure 7), since it can only be observed when the foot point crosses the extreme ultraviolet terminator. The occurrence rate is also higher over weak crustal fields, in agreement with previous studies (e.g., Brain et al., 2007; Weber et al., 2017).

3.3. Draped

As mentioned above, the effective dynamic pressure is low near the terminator so that the occurrence rate of draped (Topology 7, D-P) is not expected to be high at low altitudes, which is shown in the left column of Figure 8. The occurrence rate is higher over weak crustal fields and increases with altitude, as expected. Comparing with the other six topologies, draped is not the dominant topology below 1,000 km at most places.

4. Dominant Magnetic Topologies Over Strong and Weak Crustal Field Regions

It is instructive to examine the dominant magnetic topologies at different SZAs and altitudes by confining data within typical regions for strong and weak crustal fields, as highlighted by the white and gray boxes in the bottom left panel of Figure 8, respectively. The occurrence rate of these seven topologies for these two regions against SZA and altitude is calculated and discussed here.

4.1. Strong Crustal Field Region

Over strong crustal fields on the dayside (Figure 9), the dominant magnetic topology is draped above ~1,200 km and closed-to-day below. The effective location of the terminator as a function of SZA and altitude can be determined from the occurrence rate of the closed-void topology over strong crustal fields (Figure 9d), since the existence of a void requires that both foot points are in darkness. We calculate the terminator location as the geometric shadow of a sphere with a radius that is larger than Mars' volumetric mean radius of 3,390 km by some amount ΔH. The best separation between high and low occurrence rates of the C-V topology is achieved with $\Delta H = 120$ km (dashed black curves in Figure 9). This is located at higher SZA than the boundary for the extreme ultraviolet shadow (optical depth ≈ 1). This SZA difference gives the time scale for trapped superthermal electrons to be scattered and lost to the atmosphere, ~20 min given the planet's rotation period. There is a dawn-dusk asymmetry in Figure 9d: Voids are more extended in altitude in the dawnside than the duskside, as expected. In between closed-to-day (Figure 9a) and draped topologies (Figure 9g), there is an altitude-SZA band of moderate high occurrence rates for the open-to-day topology (Figure 9e).

There are two unexpected topologies on the dayside, closed-trapped (Figure 9c) concentrated at low SZAs and high altitudes and open-to-night (Figure 9f) scattered across a wide range of SZAs at high altitudes, both of which were anticipated to occur only on the nightside. Through examination of case studies, these trapped PAD distributions are not representative of closed field lines but anisotropic electron PADs in the sheath/magnetic pileup region (as shown in Figure 5), possibly caused by field-aligned electron loss resulting from the bow-shock-associated macroscopic and microscopic electric and magnetic fields (Feldman et al., 1983) or by perpendicular wave heating. Similarly, open-to-night (Figure 9f) occurring on the dayside is partly from pitch angle anisotropies in the sheath region and also partly from magnetic reflection by the strong magnetic pileup near the subsolar region, based on some case studies. Thus, these two outlier topologies are likely to be draped instead. Interestingly, the region ID does not identify these cases to be within the magnetosheath, probably because these outliers are more likely located at the inner side of the magnetosheath or the magnetic pileup region where it is harder to parametrize and identify. This is up for further investigation but outside of the scope of this paper.

On the nightside, the dominant magnetic topology is draped (Figure 9g) above ~1,000-km altitude, changes to closed-trapped (Figure 9c) from 600 to 1,000 km, and then to voids below 600 km. Closed-trapped
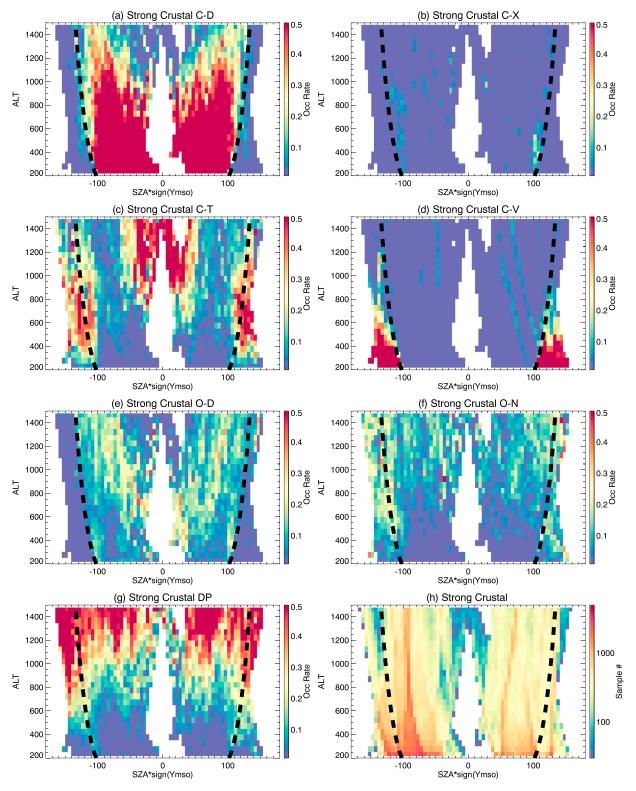
Figure 9. From left to right, top to bottom, eight panels show the occurrence rate against altitude and solar zenith angle signed by Y_{MSO}, over the strong crustal region (highlighted by the white box in the bottom left panel of Figure 8), for (a) closed-to-day (Topology 1, C-D), (b) cross-terminator closed (Topology 2, C-X), (c) closed-trapped (Topology 3, C-T), (d) voids (Topology 4, C-V), (e) open-to-day (Topology 5, O-D), (f) open-to-night (Topology 6, O-N), and (g) draped (Topology 7, DP), and (h) the total sample number of all topologies. The black dashed lines mark the terminator.
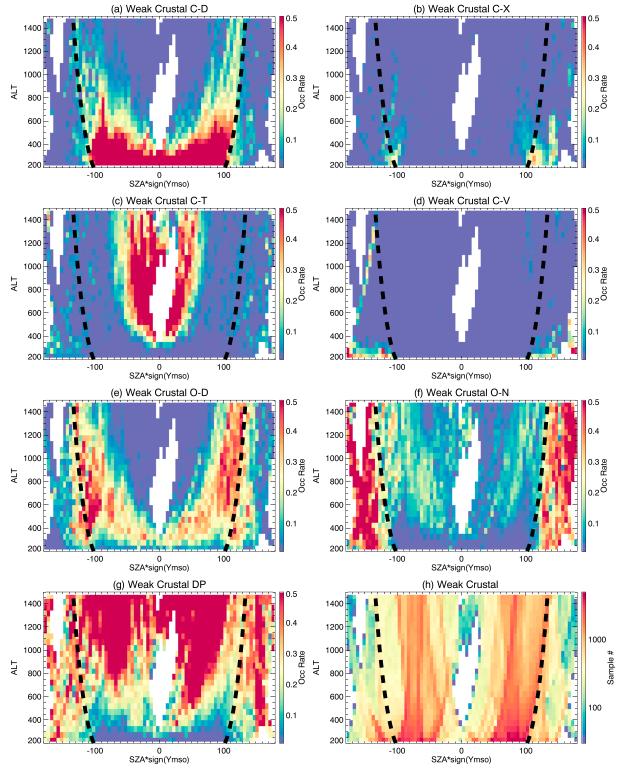
Figure 10. The same format as Figure 9 but data selected over weak crustal regions (highlighted by the two gray boxes in the bottom left panel of Figure 8).

is expected to appear when the foot points (∼160 km) of the closed loops enter darkness, which is approximately at SZA ∼100°, in agreement with the occurrence pattern for closed-trapped in Figure 9c. Open-to-night (Figure 9f) has a moderate high occurrence rate above the void-dominant altitudes (Figure 9d). Cross-terminator closed field lines (Figure 9b) are located within a narrow SZA range just sunward of the terminator.

4.2. Weak Crustal Field Region

Over weak crustal fields (Figure 10), draped (Figure 10g) dominates the dayside down to ∼400 km at low SZAs and down to ∼1,200 km near the terminator. Closed-to-day (Figure 10a) is dominant up to ∼300 km at low SZAs up to ∼600 km near the terminator. In between, open-to-day (Figure 10e) prevails, specially at SZA >∼ 60°. This is consistent with the layering scenario from Xu, Mitchell, Liemohn, et al. (2017), with closed loops at low altitudes, open-to-day originating from the periphery of strong crustal fields or the nose of deeply draped field lines near the subsolar region laying over the closed loops, and draped field lines at the top. Similar misidentification of closed-trapped (Figure 10c) and open-to-night (Figure 10f) occurs, the same as section 4.1.

On the nightside, the dominant topologies are open-to-night (Figure 10f) and draped (Figure 10g). Open-to-night (Figure 10f) has a dawn-dusk asymmetry, with a lower occurrence rate at the dusk-midnight sector than at the midnight-dawn sector, probably caused by the rotation of the planet.

Cross-terminator closed field lines (Figure 10b) over weak crustal fields are clustered near the terminator but also distributed over a much wider SZA range, compared to distribution of the same topology over strong crustal fields. A Student's t test for the two data cubes gives a significance of 1.5E−11, which demonstrates that these two distributions are significantly different. Large cross-terminator closed loops have been identified over weak crustal regions by case studies. A nightside example was identified at $SZA = 133°$ in Xu, Mitchell, et al. (2016), a dayside example at $SZA = 78°$ is shown in Figure 1e, and another dayside example at $SZA = 59°$ can be seen in case β in Figures 4 and 5 of Collinson et al. (2016). The source for photoelectron production ends approximately at SZA ∼ 100°, as stated above, which means the other foot point of these cases is located at least 33° and 22° (or 41° for the example in Collinson et al., 2016) away in SZA (∼60 km per degree). Similarly, the minimum distance between the two foot points, measured in SZA here, can be derived as the difference of the observation location and SZA ∼ 100°. Cross-terminator closed loops are small over strong crustal regions, as these field lines tend to connect with nearby strongly magnetized crust. In contrast, cross-terminator closed loops over weak crustal regions tend to be more distantly separated, probably connecting distant patches of magnetized crust. This also explains why cross-terminator closed field lines are widely spread over weak crustal regions but less so over the center of strong crustal regions (too spatially narrow to show up in mapping) in the second column of Figure 6.

5. Discussion and Conclusions

In this study, by combining two independent but complementary methods of inferring magnetic topology based on superthermal electron pitch angle and energy distributions (photoelectrons vs. solar wind origin electrons), seven magnetic topologies can be determined: four types of closed field lines (closed-to-day, cross-terminator-closed, closed-trapped, and voids), two types of open field lines (open-to-day and open-to-night), and draped field lines. This combined technique removes ambiguities in each method alone, providing a more accurate and comprehensive determination of magnetic topology than previous studies.

We apply this technique to map magnetic topology near the terminator, where all seven topologies exist. Closed-to-day dominates at low altitudes and open-to-day is found to have a high occurrence rate at higher altitudes, especially over weak crustal fields. Most open field lines with one foot point on the dayside cross the terminator and extend to nightside. These open field lines tend to cluster over weak crustal field regions and avoid strong ones. In addition, the high occurrence rate pattern of closed-trapped shifts from weaker crustal field regions to stronger crustal field regions with increasing altitude. This is because this topology is expected to be observed near the tops of closed loops, which are located at higher altitudes when crustal fields are stronger.

The dominant magnetic topologies are determined for regions of strong and weak crustal fields separately. Over strong crustal fields, draped field lines dominate high altitudes and closed-to-day dominates low alti-

tudes on the dayside, while the dominant topology changes from draped to closed-trapped and then to voids with decreasing altitude on the nightside. In contrast, a layering scenario occurs over weak crustal fields on the dayside, with closed-to-day at the bottom, open-to-day laying over that, and draped at the top. On the nightside, open-to-night and draped dominate and share similar probabilities across all altitudes.

Interestingly, cross-terminator closed field lines are confined within a narrow SZA range over the strong crustal region, as these field lines tend to have closely spaced foot points. In contrast, this topology is spread over a wide range of SZA (centered on the terminator) over weak crustal fields, suggesting widely spaced foot points connecting distant crustal patches.

References

Acuna, M., Connerney, J., Lin, R., Mitchell, D., Carlson, C., McFadden, J., et al. (1999). Global distribution of crustal magnetization discovered by the Mars Global Surveyor MAG/ER experiment. *Science*, *284*(5415), 790–793.

Acuña, M., Connerney, J., Wasilewski, P. a., Lin, R., Anderson, K., Carlson, C., et al. (1998). Magnetic field and plasma observations at Mars: Initial results of the Mars Global Surveyor mission. *Science*, *279*(5357), 1676–1680.

Acuña, M., Connerney, J., Wasilewski, P., Lin, R., Anderson, K., Carlson, C., et al. (1992). Mars Observer magnetic fields investigation. *Journal of Geophysical Research*, *97*(E5), 7799–7814.

Adams, D., Xu, S., Mitchell, D. L., Lillis, R. L., Fillingim, M., Andersson, L., et al. (2018). Using magnetic topology to probe the sources of Mars' nightside ionosphere. *Geophysical Research Letters*, *45*, 12,190–12,197. https://doi.org/10.1029/2018GL080629

Andersson, L., Ergun, R., Delory, G., Eriksson, A., Westfall, J., Reed, H., et al. (2015). The Langmuir probe and waves (LPW) instrument for MAVEN. *Space Science Reviews*, *195*(1-4), 173–198.

Bertaux, J.-L., Leblanc, F., Witasse, O., Quemerais, E., Lilensten, J., Stern, S., et al. (2005). Discovery of an aurora on Mars. *Nature*, *435*(7043), 790–794.

Brain, D., Bagenal, F., Acuña, M., & Connerney, J. (2003). Martian magnetic morphology: Contributions from the solar wind and crust. *Journal of Geophysical Research*, *108*(A12), 1424. https://doi.org/10.1029/2002JA009482

Brain, D., Halekas, J., Lillis, R., Mitchell, D., Lin, R., & Crider, D. (2005). Variability of the altitude of the Martian sheath. *Geophysical Research Letters*, *32*, L18203. https://doi.org/10.1029/2005GL023126

Brain, D., Halekas, J., Peticolas, L., Lin, R., Luhmann, J., Mitchell, D., et al. (2006). On the origin of aurora on Mars. *Geophysical Research Letters*, *33*, L01201. https://doi.org/10.1029/2005GL024782

Brain, D., Lillis, R., Mitchell, D., Halekas, J., & Lin, R. (2007). Electron pitch angle distributions as indicators of magnetic field topology near Mars. *Journal of Geophysical Research*, *112*, A09201. https://doi.org/10.1029/2007JA012435

Coates, A. J., Tsang, S., Wellbrock, A., Frahm, R., Winningham, J., Barabash, S., et al. (2011). Ionospheric photoelectrons: Comparing Venus, Earth, Mars and Titan. *Planetary and Space Science*, *59*(10), 1019–1027.

Collinson, G., Mitchell, D., Glocer, A., Grebowsky, J., Peterson, W. K., Connerney, J., et al. (2015). Electric Mars: The first direct measurement of an upper limit for the Martian "polar wind" electric potential. *Geophysical Research Letters*, *42*, 9128–9134. https://doi.org/10.1002/2015GL065084

Collinson, G., Mitchell, D., Xu, S., Glocer, A., Grebowsky, J., Hara, T., et al. (2016). Electric Mars: A large trans-terminator electric potential drop on closed magnetic field lines above Utopia Planitia. *Journal of Geophysical Research: Space Physics*, *122*, 2260–2271. https://doi.org/10.1002/2016JA023589

Connerney, J., Acuña, M., Ness, N., Kletetschka, G., Mitchell, D., Lin, R., & Reme, H. (2005). Tectonic implications of Mars crustal magnetism. *Proceedings of the national Academy of Sciences of the United States of America*, *102*(42), 14,970–14,975.

Connerney, J., Espley, J., Lawton, P., Murphy, S., Odom, J., Oliversen, R., & Sheppard, D. (2015). The MAVEN magnetic field investigation. *Space Science Reviews*, *195*, 257–291.

Connerney, J. E. P., Espley, J. R., DiBraccio, G. A., Gruesbeck, J. R., Oliversen, R. J., Mitchell, D. L., et al. (2015). First results of the MAVEN magnetic field investigation. *Geophysical Research Letters*, *42*, 8819–8827. https://doi.org/10.1002/2015GL065366

Cravens, T. E., Hamil, O., Houston, S., Bougher, S., Ma, Y., Brain, D., & Ledvina, S. (2017). Estimates of ionospheric transport and ion loss at mars. *Journal of Geophysical Research: Space Physics*, *122*, 10,626–10,637. https://doi.org/10.1002/2017JA024582

Crider, D. H., Acuña, M. H., Connerney, J. E. P., Vignes, D., Ness, N. F., Krymskii, A. M., et al. (2002). Observations of the latitude dependence of the location of the Martian magnetic pileup boundary. *Geophysical Research Letters*, *29*(8), 1170. https://doi.org/10.1029/2001GL013860

Crider, D. H., Vignes, D., Krymskii, A. M., Breus, T. K., Ness, N. F., Mitchell, D. L., et al. (2003). A proxy for determining solar wind dynamic pressure at Mars using Mars Global Surveyor data. *Journal of Geophysical Research*, *108*(A12), 1461. https://doi.org/10.1029/2003JA009875

Cui, J., Wu, X.-S., Xu, S.-S., Wang, X.-D., Wellbrock, A., Nordheim, T. A., et al. (2018). Ionization efficiency in the dayside Martian upper atmosphere. *The Astrophysical Journal Letters*, *857*(2), 7.

DiBraccio, G. A., Luhmann, J. G., Curry, S. M., Espley, J. R., Xu, S., Mitchell, D. L., et al. (2018). The twisted configuration of the Martian magnetotail: MAVEN observations. *Geophysical Research Letters*, *45*, 4559–4568. https://doi.org/10.1029/2018GL077251

Dubinin, E. M., Fraenz, M., Woch, J., Roussos, E., Winningham, J. D., Frahm, R. A., et al. (2008). Access of solar wind electrons into the Martian magnetosphere. *Annales Geophysicae*, *26*(11), 3511–3524. https://doi.org/10.5194/angeo-26-3511-2008

Dubinin, E., Fraenz, M., Woch, J., Winningham, J., Frahm, R., Lundin, R., & Barabash, S. (2008). Suprathermal electron fluxes on the nightside of Mars: Aspera-3 observations. *Planetary and Space Science*, *56*(6), 846–851.

Duru, F., Gurnett, D., Morgan, D., Winningham, J., Frahm, R., & Nagy, A. (2011). Nightside ionosphere of mars studied with local electron densities: A general overview and electron density depressions. *Journal of Geophysical Research*, *116*, A10316. https://doi.org/10.1029/2011JA016835

Eastwood, J., Brain, D., Halekas, J., Drake, J., Phan, T., Øieroset, M., et al. (2008). Evidence for collisionless magnetic reconnection at Mars. *Geophysical Research Letters*, *35*, L02106. https://doi.org/10.1029/2007GL032289

Ergun, R. E., Morooka, M. W., Andersson, L. A., Fowler, C. M., Delory, G. T., Andrews, D. J., et al. (2015). Dayside electron temperature and density profiles at Mars: First results from the MAVEN Langmuir probe and waves instrument. *Geophysical Research Letters*, *42*, 8846–8853. https://doi.org/10.1002/2015GL065280

Fang, X., Liemohn, M. W., Nagy, A. F., Ma, Y., De Zeeuw, D. L., Kozyra, J. U., & Zurbuchen, T. H. (2008). Pickup oxygen ion velocity space and spatial distribution around Mars. *Journal of Geophysical Research*, *113*, A02210. https://doi.org/10.1029/2007JA012736

Feldman, W., Anderson, R., Bame, S., Gary, S., Gosling, J., McComas, D., et al. (1983). Electron velocity distributions near the Earth's bow shock. *Journal of Geophysical Research*, *88*(A1), 96–110.

Fillingim, M., Peticolas, L., Lillis, R., Brain, D., Halekas, J., Lummerzheim, D., & Bougher, S. (2010). Localized ionization patches in the nighttime ionosphere of Mars and their electrodynamic consequences. *Icarus*, *206*(1), 112–119.

Fillingim, M. O., Peticolas, L. M., Lillis, R. J., Brain, D. A., Halekas, J. S., Mitchell, D. L., et al. (2007). Model calculations of electron precipitation induced ionization patches on the nightside of Mars. *Geophysical Research Letters*, *34*, L12101. https://doi.org/10.1029/2007GL029986

Fox, J. L., & Dalgarno, A. (1979). Ionization, luminosity, and heating of the upper atmosphere of Mars. *Journal of Geophysical Research*, *84*(A12), 7315–7333.

Frahm, R., Sharber, J., Winningham, J., Link, R., Liemohn, M., Kozyra, J., et al. (2010). Estimation of the escape of photoelectrons from Mars in 2004 liberated by the ionization of carbon dioxide and atomic oxygen. *Icarus*, *206*(1), 50–63.

Frahm, R., Sharber, J., Winningham, J., Wurz, P., Liemohn, M., Kallio, E., et al. (2006). Locations of atmospheric photoelectron energy peaks within the Mars environment. *Space Science Reviews*, *126*(1-4), 389–402.

Frahm, R., Winningham, J., Sharber, J., Scherrer, J., Jeffers, S., Coates, A., et al. (2006). Carbon dioxide photoelectron energy peaks at Mars. *Icarus*, *182*(2), 371–382.

Garnier, P., Steckiewicz, M., Mazelle, C., Xu, S., Mitchell, D., Holmberg, M. K. G., et al. (2017). The Martian photoelectron boundary as seen by MAVEN. *Journal of Geophysical Research: Space Physics*, *122*, 10,472–10,485. https://doi.org/10.1002/2017JA024497

Haider, S. A., Kim, J., Nagy, A. F., Keller, C. N., Verigin, M. I., Gringauz, K. I., et al. (1992). Calculated ionization rates, ion densities, and airglow emission rates due to precipitating electrons in the nightside ionosphere of Mars. *Journal of Geophysical Research*, *97*(A7), 10,637–10,641. https://doi.org/10.1029/92JA00317

Halekas, J., Brain, D., Luhmann, J., DiBraccio, G., Ruhunusiri, S., Harada, Y., et al. (2017). Flows, fields, and forces in the Mars-solar wind interaction. *Journal of Geophysical Research: Space Physics*, *122*, 11,320–11,341. https://doi.org/10.1002/2017JA024772

Halekas, J., Eastwood, J., Brain, D., Phan, T., Øieroset, M., & Lin, R. (2009). In situ observations of reconnection Hall magnetic fields at Mars: Evidence for ion diffusion region encounters. *Journal of Geophysical Research*, *114*, A11204. https://doi.org/10.1029/2009JA014544

Halekas, J., Ruhunusiri, S., Harada, Y., Collinson, G., Mitchell, D., Mazelle, C., et al. (2017). Structure, dynamics, and seasonal variability of the Mars-solar wind interaction: MAVEN Solar Wind Ion Analyzer in-flight performance and science results. *Journal of Geophysical Research: Space Physics*, *122*, 547–578. https://doi.org/10.1002/2016JA023167

Halekas, J., Taylor, E., Dalton, G., Johnson, G., Curtis, D., McFadden, J., et al. (2015). The Solar Wind Ion Analyzer for MAVEN. *Space Science Reviews*, *195*(1-4), 125–151.

Hall, B. E. S., Lester, M., Nichols, J. D., Sánchez-Cano, B., Andrews, D. J., Opgenoorth, H. J., & Fraenz, M. (2016). A survey of superthermal electron flux depressions, or "electron holes," within the illuminated Martian induced magnetosphere. *Journal of Geophysical Research: Space Physics*, *121*, 4835–4857. https://doi.org/10.1002/2015JA021866

Harada, Y., Andersson, L., Fowler, C. M., Mitchell, D. L., Halekas, J. S., Mazelle, C., et al. (2016). MAVEN observations of electron-induced whistler mode waves in the Martian magnetosphere. *Journal of Geophysical Research: Space Physics*, *121*, 9717–9731. https://doi.org/10.1002/2016JA023194

Harada, Y., Halekas, J. S., DiBraccio, G. A., Xu, S., Espley, J., Mcfadden, J. P., et al. (2018). Magnetic reconnection on dayside crustal magnetic fields at Mars: MAVEN observations. *Geophysical Research Letters*, *45*, 4550–4558. https://doi.org/10.1002/2018GL077281

Harada, Y., Halekas, J., McFadden, J., Espley, J., DiBraccio, G., Mitchell, D., et al. (2017). Survey of magnetic reconnection signatures in the Martian magnetotail with MAVEN. *Journal of Geophysical Research: Space Physics*, *315*, 146–157. https://doi.org/10.1016/j.icarus.2018.05.030

Jakosky, B., Brain, D., Chaffin, M., Curry, S., Deighan, J., Grebowsky, J., et al. (2018). Loss of the Martian atmosphere to space: Present-day loss rates determined from MAVEN observations and integrated loss through time. *Icarus*, *315*, 146–157. https://doi.org/10.1016/j.icarus.2018.05.030

Jakosky, B. M., Lin, R., Grebowsky, J., Luhmann, J., Mitchell, D., Beutelschies, G., et al. (2015). The Mars Atmosphere and Volatile EvolutioN (MAVEN) mission. *Space Science Reviews*, *195*(1-4), 3–48.

Leblanc, F., Witasse, O., Lilensten, J., Frahm, R. A., Safaenili, A., Brain, D. A., et al. (2008). Observations of aurorae by SPICAM ultraviolet spectrograph on board Mars Express: Simultaneous ASPERA-3 and MARSIS measurements. *Journal of Geophysical Research*, *113*, A08311. https://doi.org/10.1029/2008JA013033

Leblanc, F., Witasse, O., Winningham, J., Brain, D., Lilensten, J., Blelly, P.-L., et al. (2006). Origins of the Martian aurora observed by Spectroscopy for Investigation of Characteristics of the Atmosphere of Mars (SPICAM) on board Mars Express. *Journal of Geophysical Research*, *111*, A09313. https://doi.org/10.1029/2006JA011763

Liemohn, M. W., Frahm, R., Winningham, J., Ma, Y., Barabash, S., Lundin, R., et al. (2006). Numerical interpretation of high-altitude photoelectron observations. *Icarus*, *182*(2), 383–395.

Liemohn, M. W., Ma, Y., Frahm, R. A., Fang, X., Kozyra, J. U., Nagy, A. F., et al. (2006). Mars global MHD predictions of magnetic connectivity between the dayside ionosphere and the magnetospheric flanks. *Space Science Reviews*, *126*, 63–76. https://doi.org/10.1007/s11214-006-9116-8

Liemohn, M. W., Ma, Y., Nagy, A., Kozyra, J., Winningham, J., Frahm, R., et al. (2007). Numerical modeling of the magnetic topology near Mars auroral observations. *Geophysical Research Letters*, *34*, L24202. https://doi.org/10.1029/2007GL031806

Liemohn, M. W., Mitchell, D. L., Nagy, A. F., Fox, J. L., Reimer, T. W., & Ma, Y. (2003). Comparisons of electron fluxes measured in the crustal fields at Mars by the MGS Magnetometer/Electron Reflectometer instrument with a B field–dependent transport code. *Journal of Geophysical Research*, *108*(E12), 5134. https://doi.org/10.1029/2003JE002158

Liemohn, M. W., & Xu, S. (2018). Recent advances regarding the mars magnetotail current sheet. *Electric Currents in Geospace and Beyond*, *235*, 177–190. https://doi.org/10.1002/9781119324522.ch11

Liemohn, M. W., Xu, S., Dong, C., Bougher, S. W., Johnson, B. C., Ilie, R., & De Zeeuw, D. L. (2017). Ionospheric control of the dawn-dusk asymmetry of the Mars magnetotail current sheet. *Journal of Geophysical Research: Space Physics*, *122*, 6397–6414. https://doi.org/10.1002/2016JA023707

Lillis, R. J., & Brain, D. A. (2013). Nightside electron precipitation at Mars: Geographic variability and dependence on solar wind conditions. *Journal of Geophysical Research: Space Physics*, *118*, 3546–3556. https://doi.org/10.1002/jgra.50171

Lillis, R. J., Fillingim, M. O., & Brain, D. A. (2011). Three-dimensional structure of the Martian nightside ionosphere: Predicted rates of impact ionization from Mars Global Surveyor Magnetometer and Electron Reflectometer measurements of precipitating electrons. *Journal of Geophysical Research*, *116*, A12317. https://doi.org/10.1029/2011JA016982

Lillis, R. J., Fillingim, M. O., Peticolas, L. M., Brain, D. A., Lin, R. P., & Bougher, S. W. (2009). Nightside ionosphere of Mars: Modeling the effects of crustal magnetic fields and electron pitch angle distributions on electron impact ionization. *Journal of Geophysical Research*, *114*, E11009. https://doi.org/10.1029/2009JE003379

Lillis, R. J., Mitchell, D. L., Steckiewicz, M., Brain, D., Xu, S., Weber, T., et al. (2018). Ionizing electrons on the Martian nightside: Structure and variability. *Journal of Geophysical Research: Space Physics*, *123*, 4349–4363. https://doi.org/10.1029/2017JA025151

Luhmann, J., Dong, C., Ma, Y., Curry, S., Mitchell, D., Espley, J., et al. (2015). Implications of MAVEN Mars near-wake measurements and models. *Geophysical Research Letters*, *42*, 9087–9094. https://doi.org/10.1002/2015GL066122

McFadden, J., Kortmann, O., Curtis, D., Dalton, G., Johnson, G., Abiad, R., et al. (2015). MAVEN SupraThermal And Thermal Ion Composition (STATIC) instrument. *Space Science Reviews*, *195*(1-4), 199–256.

Mitchell, D., Lillis, R., Lin, R., Connerney, J., & Acuña, M. (2007). A global map of Mars' crustal magnetic field based on electron reflectometry. *Journal of Geophysical Research*, *112*, E01002. https://doi.org/10.1029/2005JE002564

Mitchell, D., Lin, R., Mazelle, C., Reme, H., Cloutier, P., Connerney, J., et al. (2001). Probing Mars' crustal magnetic field and ionosphere with the MGS Electron Reflectometer. *Journal of Geophysical Research*, *106*(E10), 23,419–23,427.

Mitchell, D., Lin, R., Reme, H., Crider, D., Cloutier, P., Connerney, J., et al. (2000). Oxygen Auger electrons observed in Mars' ionosphere. *Geophysical research letters*, *27*(13), 1871–1874.

Mitchell, D., Mazelle, C., Sauvaud, J.-A., Thocaven, J.-J., Rouzaud, J., Fedorov, A., et al. (2016). The MAVEN Solar Wind Electron Analyzer. *Space Science Reviews*, *200*(1-4), 495–528.

Morschhauser, A., Lesur, V., & Grott, M. (2014). A spherical harmonic model of the lithospheric magnetic field of Mars. *Journal of Geophysical Research: Planets*, *119*, 1162–1188. https://doi.org/10.1002/2013JE004555

Peterson, W., Thiemann, E., Eparvier, F. G., Andersson, L., Fowler, C., Larson, D., et al. (2016). Photoelectrons and solar ionizing radiation at Mars: Predictions versus MAVEN observations. *Journal of Geophysical Research: Space Physics*, *121*, 8859–8870. https://doi.org/10.1002/2016JA022677

Sakai, S., Andersson, L., Cravens, T. E., Mitchell, D. L., Mazelle, C., Rahmati, A., et al. (2016). Electron energetics in the Martian dayside ionosphere: Model comparisons with MAVEN data. *Journal of Geophysical Research: Space Physics*, *121*, 7049–7066. https://doi.org/10.1002/2016JA022782

Sakai, S., Rahmati, A., Mitchell, D. L., Cravens, T. E., Bougher, S. W., Mazelle, C., et al. (2015). Model insights into energetic photoelectrons measured at Mars by MAVEN. *Geophysical Research Letters*, *42*, 8894–8900. https://doi.org/10.1002/2015GL065169

Schneider, N. M., Deighan, J. I., Jain, S. K., Stiepen, A., Stewart, A. I. F., Larson, D., et al. (2015). Discovery of diffuse aurora on Mars. *Science*, *350*(6261), aad0313.

Schneider, N. M., Jain, S. K., Deighan, J., Nasr, C. R., Brain, D. A., Larson, D., et al. (2018). Global aurora on Mars during the September 2017 space weather event. *Geophysical Research Letters*, *45*, 7391–7398. https://doi.org/10.1029/2018GL077772

Seth, S. P., Haider, S. A., & Oyama, K. I. (2002). Photoelectron flux and nightglow emissions of 5577 and 6300 Å due to solar wind electron precipitation in Martian atmosphere. *Journal of Geophysical Research*, *107*, 1324. https://doi.org/10.1029/2001JA000261

Shane, A. D., Xu, S., Liemohn, M. W., & Mitchell, D. L. (2016). Mars nightside electrons over strong crustal fields. *Journal of Geophysical Research: Space Physics*, *121*, 3808–3823. https://doi.org/10.1002/2015JA021947

Steckiewicz, M. (2017). The nightside ionosphere of Mars unveiled by suprathermal electron depletions (Ph.D. thesis), Université Toulouse 3 Paul Sabatier (UT3 Paul Sabatier).

Steckiewicz, M., Garnier, P., André, N., Mitchell, D. L., Andersson, L., Penou, E., et al. (2017). Comparative study of the Martian suprathermal electron depletions based on Mars Global Surveyor, Mars Express, and Mars Atmosphere and Volatile EvolutioN mission observations. *Journal of Geophysical Research: Space Physics*, *122*, 857–873. https://doi.org/10.1002/2016JA023205

Steckiewicz, M., Mazelle, C., Garnier, P., Andr, N., Penou, E., Beth, A., et al. (2015). Altitude dependence of nightside Martian suprathermal electron depletions as revealed by MAVEN observations. *Geophysical Research Letters*, *42*, 8877–8884. https://doi.org/10.1002/2015GL065257

Ulusen, D., Brain, D. A., & Mitchell, D. L. (2011). Observation of conical electron distributions over Martian crustal magnetic fields. *Journal of Geophysical Research*, *116*, A07214. https://doi.org/10.1029/2010JA016217

Vignes, D., Mazelle, C., Rme, H., Acuña, M. H., Connerney, J. E. P., Lin, R. P., et al. (2000). The solar wind interaction with Mars: Locations and shapes of the bow shock and the magnetic pile-up boundary from the observations of the MAG/ER Experiment onboard Mars Global Surveyor. *Geophysical Research Letters*, *27*, 49–52. https://doi.org/10.1029/1999GL010703

Weber, T., Brain, D., Mitchell, D., Xu, S., Connerney, J., & Halekas, J. (2017). Characterization of low-altitude nightside Martian magnetic topology using electron pitch angle distributions. *Journal of Geophysical Research: Space Physics*, *122*, 9777–9789. https://doi.org/10.1002/2017JA024491

Xu, S., Fang, X., Mitchell, D. L., Ma, Y., Luhmann, J. G., DiBraccio, G. A., et al. (2018). Investigation of Martian magnetic topology response to 2017 September ICME. *Geophysical Research Letters*, *45*, 7337–7346. https://doi.org/10.1029/2018GL077708

Xu, S., & Liemohn, M. W. (2015). Superthermal electron transport model for Mars. *Earth and Space Science*, *2*, 47–64. https://doi.org/10.1002/2014EA000043

Xu, S., Liemohn, M., Bougher, S., & Mitchell, D. (2015). Enhanced carbon dioxide causing the dust storm-related increase in high-altitude photoelectron fluxes at Mars. *Geophysical Research Letters*, *42*, 9702–9710. https://doi.org/10.1002/2015GL066043

Xu, S., Liemohn, M., Bougher, S., & Mitchell, D. (2016). Martian high-altitude photoelectrons independent of solar zenith angle. *Journal of Geophysical Research: Space Physics*, *121*, 3767–3780. https://doi.org/10.1002/2015JA022149

Xu, S., Liemohn, M. W., & Mitchell, D. L. (2014). Solar wind electron precipitation into the dayside Martian upper atmosphere through the cusps of strong crustal fields. *Journal of Geophysical Research: Space Physics*, *119*, 10,100–10,115. https://doi.org/10.1002/2014JA020363

Xu, S., Liemohn, M. W., Peterson, W., Fontenla, J., & Chamberlin, P. (2015). Comparison of different solar irradiance models for the superthermal electron transport model for Mars. *Planetary and Space Science*, *119*, 62–68.

Xu, S., Mitchell, D., Liemohn, M., Dong, C., Bougher, S., Fillingim, M., et al. (2016). Deep nightside photoelectron observations by MAVEN SWEA: Implications for Martian northern hemispheric magnetic topology and nightside ionosphere source. *Geophysical Research Letters*, *43*, 8876–8884. https://doi.org/10.1002/2016GL070527

Xu, S., Mitchell, D., Liemohn, M., Fang, X., Ma, Y., Luhmann, J., et al. (2017). Martian low-altitude magnetic topology deduced from MAVEN/SWEA observations. *Journal of Geophysical Research: Space Physics*, *122*, 1831–1852. https://doi.org/10.1002/2016JA023467

Xu, S., Mitchell, D., Luhmann, J., Ma, Y., Fang, X., Harada, Y., et al. (2017). High-altitude closed magnetic loops at Mars observed by MAVEN. *Geophysical Research Letters*, *44*, 11,229–11,238. https://doi.org/10.1002/2017GL075831

Xu, S., Mitchell, D. L., McFadden, J. P., Collinson, G., Harada, Y., Lillis, R., et al. (2018). Field-aligned potentials at Mars from MAVEN observations. *Geophysical Research Letters*, *45*, 10,119–10,127. https://doi.org/10.1029/2018GL080136

Xu, S., Thiemann, E., Mitchell, D., Eparvier, F., Pawlowski, D., Benna, M., et al. (2018). Observations and modeling of the Mars low-altitude ionospheric response to the 10 September 2017 X-class solar flare. *Geophysical Research Letters*, *45*, 7382–7390. https://doi.org/10.1029/2018GL078524